INFRARED IMAGING OF THE LARGE MAGELLANIC CLOUD STAR-FORMING REGION HENIZE 206

V. Gorjian and M W. Werner

Jet Propulsion Laboratory, MC 169-327, California Institute of Technology, 4800 Oak Grove Drive, Pasadena, CA 91109; varoujan.gorjian@jpl.nasa.gov

J. R. Mould

National Optical Astronomy Observatory, P.O. Box 26732, 950 North Cherry Avenue, Tucson, AZ 85726-6732

K. D. Gordon, J. Muzzerole, and J. Morrison

Steward Observatory, University of Arizona, Tucson, AZ 85721

J. M. Surace, L. M. Rebull, and R. L. Hurt

Spitzer Science Center, California Institute of Technology, MC 220-6, 1200 East California Boulevard, Pasadena, CA 91125

R. C. Smith, S. D. Points, and C. Aguilera

Cerro Tololo Inter-American Observatory, Casilla 603, La Serena, Chile

J. M. De Buizer

Gemini Observatory, Casilla 603, La Serena, Chile

and

C. Packham

Department of Astronomy, University of Florida, Gainesville, FL 32611

ABSTRACT

Henize 206 is a region of star formation in the Large Magellanic Cloud of the approximate scale of the Orion belt and sword. Our *Spitzer Space Telescope* infrared images and Cerro Tololo Inter-American Observatory (CTIO) optical images show that the region is experiencing very energetic star formation. The radiation from young stars has excited strong polycyclic aromatic hydrocarbon (PAH) emission throughout Henize 206, except on the side of the nebula with the prominent young supernova remnant. As is also seen in early *Spitzer* observations of M81, star formation rates calculated from Hα for Henize 206 may miss the deeply embedded young stars, compared with star formation rates calculated from far infrared emission. For one of the highest surface brightness regions of Henize 206, we obtained snapshot exposures with the Thermal-Region Camera Spectrograph on Gemini South to explore the complex structure. A few percent of the total flux from this brightest region in Henize 206 emanates from infrared peaks of subparsec scale.

Subject headings: infrared: galaxies — infrared: stars — Magellanic Clouds — stars: formation

1. INTRODUCTION

Henize 206 (He 206; aka LHA 120-N 206 and DEM L 221) is a high-mass star-forming region on the outskirts of the Large Magellanic Cloud (LMC) that surrounds the star-forming cluster NGC 2018 (LHA 120-N 206A). It was first cataloged in an Hα objective prism survey by Karl Henize in 1956 (Henize 1956). The current star formation is taking place around an X-ray superbubble, which is a result of either stellar superwinds or a supernova (Dunne et al. 2001). As there are no obvious stars producing superwinds at this time, it is more likely a supernova remnant. There is an H I shell that is co-incident with the X-ray superbubble that has an expansion velocity of 22.5 km s^{-1} (Kim et al. 1999), leading to an estimate for the age of the shell of 2.8×10^6 yr. Bica et al. (1996) used *UBV* photometry to set an upper limit of 10 Myr for the age of the stars in the region; therefore, if the star formation was triggered by the impact of the shock wave from the supernova, their ages must be somewhere between $\sim$2 and 10 million yr old.

What is intriguing about He 206 (and all star formation in the LMC) is the fact that the LMC has lower metallicity than the Milky Way ([Fe/H] $= -0.31 \pm 0.04$ or 49% of solar; Rolleston et al. 2002). However, unlike young, high-redshift, starburst galaxies, the LMC is close enough for us to pick out individual star-forming regions and study them in great detail at a wide range of wavelengths. This proximity, combined with the resolution and sensitivity of the *Spitzer Space Telescope*, provides a great opportunity to study low-metallicity star formation at distances of kiloparsecs instead of gigaparsecs.

2. OBSERVATIONS

Both the Infrared Array Camera (IRAC; Fazio et al. 2004) and the Multiband Imager and Photometer for *Spitzer* (MIPS; Rieke et al. 2004) were used to create a multiwavelength image of He 206. For IRAC (3.6, 4.5, 5.8, and 8 μm); a four-column by five-row mosaic was created to cover a final region $20' \times 20'$, with three, 12 s dithers, resulting in a total exposure time of 36 s at each location and at each wavelength. The IRAC images were reduced using the standard *Spitzer* Science Center (SSC) data pipeline to produce Basic Calibrated Data (BCD), which were then mosaicked to get the final images. The final IRAC photometry is accurate to 10%.

The MIPS scan map observations were taken at a medium scan rate, consisting of eight scan legs with 148″ offsets between each pair of legs. The final MIPS images cover $0°.5 \times 20'$ and have a total exposure time of 80, 40, and 8 s per point for 24, 70, and 160 μm, respectively. The MIPS images were reduced using the MIPS Instrument Team Data Analysis

TABLE 1
Henize 206 Fluxes

Name	R.A. (J2000.0)	Decl. (J2000.0)	Aperture Size	3.6 μm (Jy)	4.5 μm (Jy)	5.8 μm (Jy)	8.0 μm (Jy)	24 μm (Jy)	70 μm (Jy)	160 μm (Jy)
He 206 Bar	05 30 55.0	−71 06 30	11′ × 7′	2.8	2.0	10.2	26.9	171	510	1190
He 206 I	05 31 22.8	−71 04 10	20″ radius	0.06	0.04	0.15	0.44	2.7	13.7	15.4
He 206 II..................	05 30 21.2	−71 07 44	20″ radius	0.03	0.02	0.09	0.26	1.5	7.6	11.8
He 206 III	05 30 48.0	−71 07 49	40″ radius	0.04	0.03	0.12	0.36	4.2	37.3	111.3

Notes.—Units of right ascension are hours, minutes, and seconds, and units of declination are degrees, arcminutes, and arcseconds. For all the IRAC sources appropriate corrections have been applied to account for the difference between point source and diffuse source calibration. The correction factors at each wavelength are 3.6 μm = 0.94, 4.5 μm = 0.94, 5.8 μm = 0.63, and 8.0 μm = 0.69. Aperture corrections have been applied to the MIPS values: For 20″ radius the aperture corrections are 24 μm = 1.12, 70 μm = 1.59, and 160 μm = 2.27; for 40″ radius the aperture corrections are 24 μm = 1.10, 70 μm = 1.11, and 160 μm = 1.52. Sky subtraction for all wavelengths was done on a 3 pixel annulus immediately outside the photometry aperture to remove the nearby diffuse contribution. The 3.6–8.0 μm fluxes have errors of 10%, while the 24, 70, and 160 μm fluxes have errors of 10%, 20%, and 20%, respectively.

Tool (DAT), which is the test bed for data reduction algorithms for MIPS (Gordon et al. 2004). The reduction of the 24 μm images followed the preflight expectations. The 70 μm reductions deviated significantly from preflight expectations requiring a time-dependent illumination correction, stim flash latent correction, and background removal. The 160 μm reduction followed preflight expectations, except it did not require stim flash latent correction. Because of the preliminary nature of the characterization of Ge arrays at this date, a few preflight reduction steps have not been implemented fully (e.g., electronic and flux nonlinearities). The uncertainties in the final MIPS photometry are estimated at 10%, 20%, and 20% for the 24, 70, and 160 μm data, respectively.

Flux extraction was done in four regions, the three brightest emitting regions from 3.6 to 160 μm, which we have labeled as sources I through III, and the overall star formation bar (see Fig. 1 [Plate 1]). All coordinates are noted in Table 1. The bar extraction was over a 11′ × 7′ region. The aperture extraction radii for source I (aka NGC 2018) and source II are 20″, which cover the 40″ FWHM *Spitzer* beam at 160 μm; source III is larger than a single 160 μm beam and thus required a larger aperture radius of 40″. Appropriate correction factors have been applied to all four wavelengths to account for the difference between point source and diffuse flux calibrations. Background subtraction for all wavelengths was done on an annulus immediately outside the photometry aperture to remove the nearby diffuse contribution.

The optical images were obtained at the University of Michigan/Cerro-Tololo Inter American Observatories' (CTIO) Curtis Schmidt telescope as part of the Magellanic Cloud Emission Line Survey. The field of view for the final image was 1°.1 × 1°.1, with exposure times of 1200, 600, and 1200 s for the [O III], Hα, and [S II] filters, respectively. Bad-column and cosmic-ray removal were done in a standard CCD reduction technique. The final photometric accuracy is 10%. The Hα flux for source I was derived in a similar aperture to the IR (20″ radius) with sky subtraction done immediately outside the photometry aperture. Sources II and III are barely detected in Hα.

3. IMAGES

Figure 1 shows a composite IRAC/MIPS 24 μm image of He 206, as well the optical, IRAC, and MIPS 24 μm images individually. The presence of multiple bright 24 μm sources is a good indicator that a great deal of star formation is going on in a bar that extends from the northeast to the southwest. Most of the embedded star-forming sources do not have counterparts

in the optical. In addition, there is some IR emission from a ring of material on the outskirts of the main optical emission.

Figure 2 (Plate 2) is a three-panel representation of the MIPS 24, 70, and 160 μm images. The 24 μm image resembles the IRAC 8 μm image, but the 160 μm image has significant emission from a north-south extended region that is ~2′ long, which we have labeled source III. The emission is from dust that is cooler than the 24 μm emitting dust. The presence and extent of source III indicates variations in dust heating and density within the bar.

The star formation bar has an extent of 11′ × 7′, which corresponds to 160 × 100 pc and an area of 1.6×10^4 pc^2 at a distance of 50 kpc (Sandage & Bedke 1994). The spectral energy distributions (SEDs) of the bar and sources I through III are plotted in Figure 3. Between 3.6 and 4.5 μm, all the sources show a dip, which is likely due to a photospheric contribution at 3.6 μm. For the bar region a lot of that photospheric contribution comes from foreground stars. What is noteworthy is that in the dust-dominated wavelengths longer than 4.5 μm, even though the warm, compact sources (I and II)
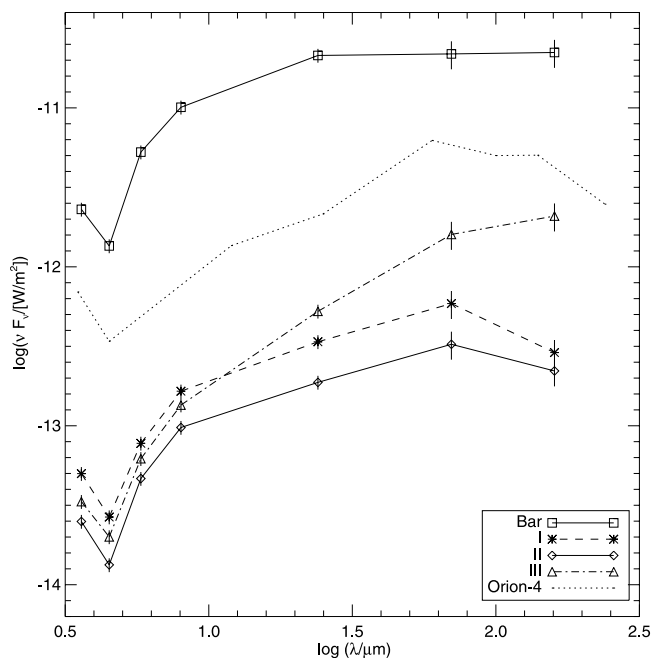

Fig. 3.—SEDs of the star-forming bar, sources I through III, and the Orion belt and sword region. The Orion values have been shifted for easier comparison with the He 206 values.
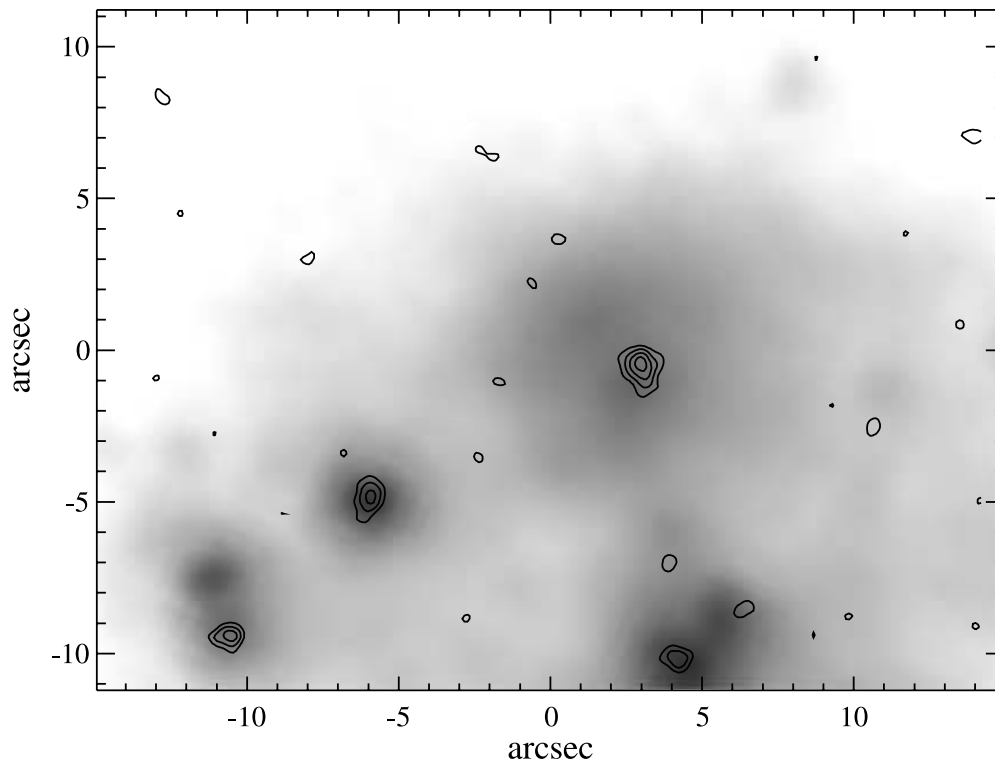
FIG. 4.—Source II contour plot overlay of Gemini T-ReCS high-resolution 11.7 μm image on the IRAC 3.6 μm image. North is up, and east is to the left. From west to east the source flux densities are 9, 21, 10, and 12 mJy ($\pm25\%$).

contribute very little to the overall flux, the colors of the large-scale measurement and the compact sources are similar out to 24 μm. The SEDs deviate significantly beyond 24 μm where the bar shows a flat slope, while sources I and II show a rise and then a dip.

It is intriguing that the SEDs on parsec scales are largely similar to those on 100 pc scales. A possible explanation may be that throughout the source the $\sim$4–25 μm radiation is nonequilibrium emission from transiently heated grains or macromolecules. In this case the SED can be independent of energy density and thus fairly uniform across the region. It will be interesting to pursue this up to the scale of galaxies.

It is instructive to compare He 206 to a more familiar, young star-forming region, to provide a baseline of comparison for the energetics of the system. The Orion belt and sword (M42, M43, and the nebulosity around σ Orionis) are young (<10 Myr; e.g., Rebull et al. 2000) and have a 12–100 μm luminosity of 4×10^5 $L_{\odot}$.[1] He 206 has an 8–160 μm luminosity of 6×10^6 $L_{\odot}$, which when interpolated from 12 to 100 μm gives a value of 4×10^6 $L_{\odot}$, a factor of 10 higher than Orion. The 157 deg^2 region of Orion has a physical scale of 1.02×10^4 pc^2, which makes it similar in size to He 206. The comparable size but higher IR luminosity of He 206 serves to highlight the very energetic nature of the star formation that is occurring there.

Another interesting difference is in the SEDs. Orion's overall SED is similar to the SEDs of the much smaller sources I and II, which have a peak at 70 μm and then a dip at 160 μm. He 206 shows a rise from 8 to 24 μm and then a flat slope out to 160 μm. These differences suggest a broader dust temperature

distribution that extends to somewhat lower temperatures in He 206 than in Orion.

An additional interesting feature is a possible lack of polycyclic aromatic hydrocarbon (PAH) emission from the northeast side of the nebula as represented by the green color (8 μm filter that spans the PAH emission feature) in Figure 1, although there is no lack of dust emission as evidenced by the red 24 μm emission. Since the optical image has a large amount of Hα emission in that direction, a lack of exciting photons seems unlikely to be the cause of the PAH emission deficit. This lack of emission may be due to the ionization state or even the absence of PAHs themselves. The PAHs may have been depleted by the nearby supernova or by high-energy UV photons from NGC 2018 (source I).

4. GEMINI EXPLORATORY IMAGING

For the high surface brightness region labeled source II, on 2004 January 30 we obtained snapshot exposures with the mid-IR camera Thermal-Region Camera Spectrograph (T-ReCS) on Gemini South to explore its complex structure. The contours in Figure 4 are from the 11.7 μm ($\Delta\lambda = 1.13$ μm) image that had an on-source exposure time of 240 s. From west to east the source flux densities are 9, 21, 10, and 12 mJy, with the faintest source being just detected with a signal-to-noise ratio $\sim$5 in this short exposure. α Carina was used as the calibration standard with an assumed flux density of 108 Jy at 11.7 μm; the calibration uncertainty is $\pm25\%$.

The 8–160 μm luminosity of source II is 7×10^4 $L_{\odot}$, which is 1% that of the full star-forming bar. The Gemini images suggest that this luminosity is provided by four deeply embedded sources of subparsec scale. Thus, each would have a luminosity $\sim$2 $\times 10^4$ $L_{\odot}$, comparable to that of the B stars that produce much of the emission from the Orion region.

---

[1] The Orion belt and sword values are from DIRBE (Wall et al. 1996) for two 10° diameter regions containing the Orion A and Orion B molecular clouds with an area of 157 deg^2 at a distance of 450 pc.

5. STAR FORMATION RATES

In a review of star formation in different galaxy types, Kennicutt (1998) offered two formulae for deriving star formation rates (SFRs) for star-forming galaxies based on different observables. His equation (2) relates Hα luminosity to SFR: SFR($M_\odot$ yr^{-1}) = $7.9 \times 10^{-42} L$(Hα) (ergs s^{-1}). His equation (4) relates far-IR (8–1000 μm) luminosity to SFR: SFR($M_\odot$ yr^{-1}) = $4.5 \times 10^{-44} L_{\rm FIR}$ (ergs s^{-1}). In the spirit of § 4 it is interesting to examine the applicability of this macroscopic estimator to individual star-forming regions.

Source I has an Hα luminosity of 3.1×10^{36} ergs s^{-1}, which gives an SFR of 2×10^{-5} $M_\odot$ yr^{-1}. In the IR, we only have coverage from 8 to 160 μm, and not the 8–1000 μm average adopted by Kennicutt, but the majority of the luminosity from star formation comes at wavelengths shorter than 160 μm (Dale & Helou 2002). For source I, $L_{\rm FIR} = 2.9 \times 10^{38}$ ergs s^{-1}, predicting an SFR of 1×10^{-5} $M_\odot$ yr^{-1}. So both methods give similar results.[2]

SFR measurements from Hα alone are more limited, however. Sources II and III are enshrouded by dust and do not have significant Hα flux. Note also that if a star-forming region like He 206 were unresolved in a far away galaxy, a large amount of Hα emission from the X-ray superbubble would be combined with that from star formation, leading to an exaggerated SFR.

To calculate the overall SFR for He 206, we have used the FIR luminosity of 2.2×10^{40} ergs s^{-1}, which yields an SFR of 1×10^{-3} $M_\odot$ yr^{-1}. Extinction-related differences in the SFR derived from Hα and the FIR are also seen in M81 (see Gordon et al. 2004).

6. SUMMARY

1. He 206 is a star-forming region that is similar in size to the belt and sword of Orion but is a factor ~10 more luminous in the IR. This highlights the very energetic star formation that is occurring.

2. The SED of the Orion region is different from He 206. This is most likely because He 206 has a broader dust temperature distribution.

3. Shortward of 30 μm, the SED of the overall region is a good representation of the SEDs of each individual compact star-forming regions. However, these regions contribute a very small part of the total flux. This may be attributable to non-equilibrium heating of the dust.

4. High-resolution ground-based follow-up of one of the compact regions with the Gemini telescope using T-ReCS has identified individual sources at 11.7 μm that may have luminosities similar to those of early-type B stars, making them analogs to the excitation sources in Orion.

5. The Hα and FIR luminosities give similar SFR results for source I, which does not have a significant amount of enshrouding dust, but for dust-enshrouded sources, the FIR luminosity is a more reliable predictor of SFR. The SFR of the region is 1×10^{-3} $M_\odot$ yr^{-1} based on the FIR luminosity of He 206.

---

[2] Typical internal reddedning for H II regions in the LMC is $E(B - V) = 0.2$ (Bica et al. 1996), which translates into an $A_V = 0.6$–0.8 and an $A_R = 0.5$–0.6. So dust extinction should not be a significant factor in the calculation of the SFR from the Hα luminosity. This is supported by the similar values derived for the SFR for Source I from the Hα and the IR.

REFERENCES

Bica, E., Claria, J. J., Dottori, H., Santos, J. F. C., & Piatti, A. E. 1996, ApJS, 102, 57
Dale, D. A., & Helou, G. 2002, ApJ, 576, 159
Dunne, B. C., Points, S. D., & Chu, Y. 2001, ApJS, 136, 119
Fazio, G. G., et al. 2004, ApJS, 154, 10
Gordon, K. D., et al. 2004, ApJS, 154, 215
Henize, K. G. 1956, ApJS, 2, 315
Kennicutt, R. C. 1998, ARA&A, 36, 189

Kim, S., Dopita, M. A., Staveley-Smith, L., & Bessell, M. S. 1999, AJ, 118, 2797
Rebull, L. M., Hillenbrand, L. A., Strom, S. E., Duncan, D. K., Patten, B. M., Pavlovsky, C. M., Makidon, R., & Adams, M. T. 2000, AJ, 119, 3026
Rolleston, W. R. J., Trundle, C., & Dufton, P. L. 2002, A&A, 396, 53
Sandage, A. & Bedke, J. 1994, The Carnegie Alas of Glaxies (Washington: Carnegie Inst.)
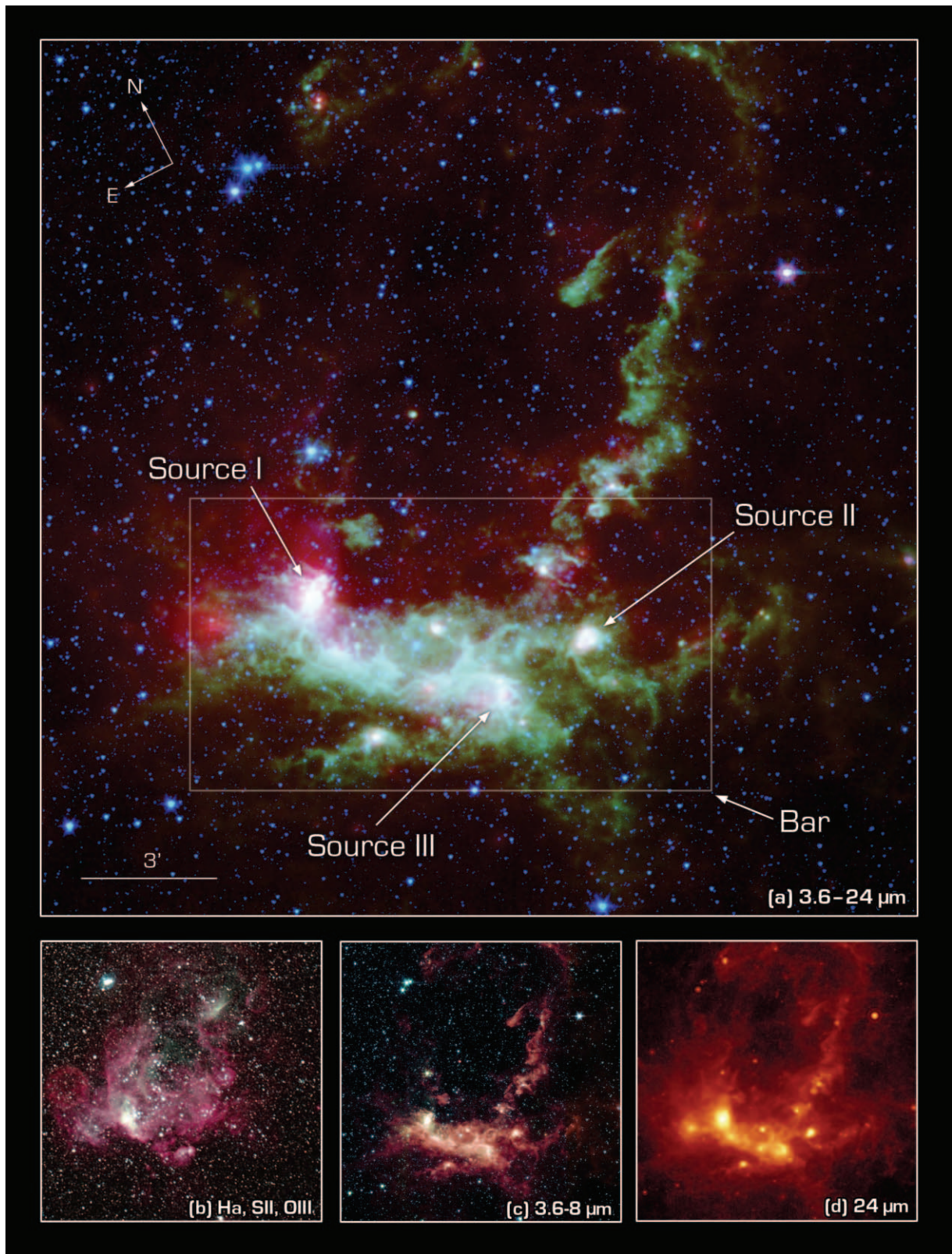Wall, W. F., et al. 1996, ApJ, 456, 566

FIG. 1.—(a) Composite of IRAC and MIPS data from 3.6 to 24 μm. Blue represents 3.6 and 4.5 μm. Note that most of the stars in the field of view radiate primarily at these short-infrared wavelengths. Cyan denotes emission at 5.8 μm, green depicts the 8.0 μm light, and red is used to trace the thermal emission from dust at 24 μm. (b) An optical image from CTIO showing a true color representation of the Hα, [S II], and [O III] emission lines. Note that the Hα comes not only from the star formation region but also the central X-ray superbubble, which may be the result of a supernova. There is another smaller supernova remnant on the left (eastern) side of the star formation bar very prominent in [S II] emission. (c) Composite IRAC image from 3.6 to 8 μm. (d) MIPS 24 μm image.
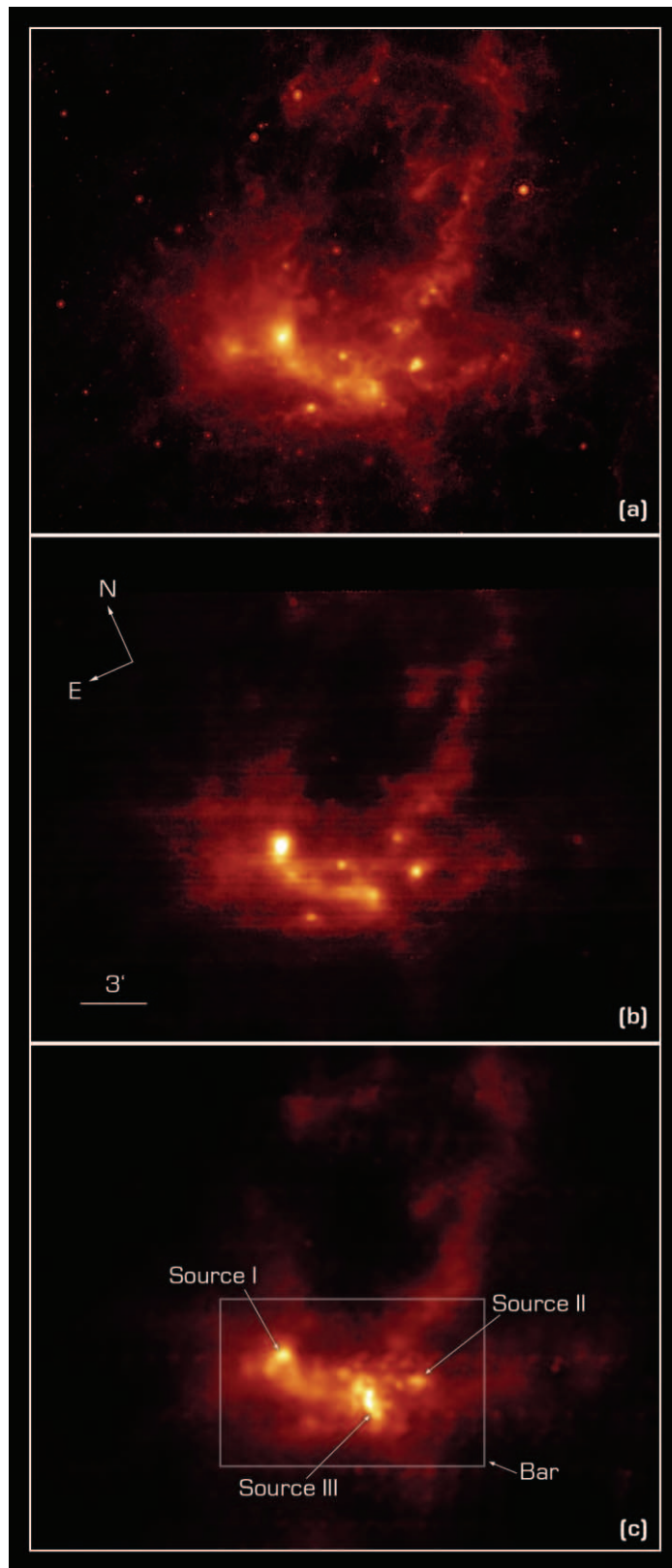
PLATE 1

Fig. 2.—Panels *a*, *b*, and *c* represent the MIPS 24, 70, and 160 μm images, respectively. Note the cool region marked as source III, which is very prominent at 160 μm.

PLATE 2